High Temperature Corrosion of Materials (2023) 100:655–682
https://doi.org/10.1007/s11085-023-10192-0

ORIGINAL PAPER

Corrosion Behaviour of Fe-Based and Ni-Based Alloys in Wet CO_2 Gas with and without Chloride Deposits at 750 °C

Yuchen Cai[1] · Zhe Zhang[1] · Jianqiang Zhang[1] · Brian Gleeson[2] · David J. Young[1]

Received: 12 June 2023 / Revised: 6 September 2023 / Accepted: 8 September 2023 /
Published online: 29 September 2023

Abstract

Corrosion behaviours of Fe–25Cr, Fe–25Cr–2Mn–1Si, Fe–25Cr–20Ni, 310SS, Ni–25Cr, and Ni–25Cr–2Mn–1Si (all in wt%) with and without NaCl–KCl deposits in Ar–60%CO_2–20%H_2O gas at 750 °C were studied. Without salt deposits, Fe–25Cr performed protectively, while Fe–25Cr–20Ni and Ni–25Cr underwent breakaway oxidation with multilayered scales formed. Adding alloy elements Si + Mn increased the corrosion resistance of all alloys by forming additional Mn-rich oxides and silica. Surface deposits of NaCl–KCl accelerated corrosion, forming porous Fe-rich oxide nodules for Fe–25Cr and thick, porous scales and internal oxidation zones for all other alloys. The protective effect of Si + Mn alloying disappeared in the presence of chlorides. Limited intergranular carbides were observed for all alloys in the gas-only condition. The extent of carburisation increased with the presence of chloride deposits for all Fe-based alloys, but remained unchanged for Ni-based alloys. Corrosion of these alloys at 750 °C is compared with that at 650 °C. The effect of chlorides in volatilising metals at 750 °C is discussed.

Keywords Alloy · High-temperature corrosion · Alloying effect · Chloride

Introduction

Reducing carbon emissions is a current global trend in attempting to limit global warming. Although renewable and clean energy sources are increasingly utilised, the traditional fossil fuel energy could remain in use for decades due to the

✉ Jianqiang Zhang
j.q.zhang@unsw.edu.au

[1] School of Materials Science and Engineering, University of New South Wales, Sydney, NSW 2052, Australia

[2] Department of Mechanical Engineering and Materials Science, University of Pittsburgh, Pittsburgh, PA 15261, USA

enormous energy demand. Oxy-fuel combustion is a potential technology for limiting CO_2 emissions in thermal power generation. In this process, coal is burnt in oxygen diluted with recycled flue gas, instead of air, which therefore produces flue gas mainly consisting of CO_2 and H_2O, allowing easier CO_2 collection and sequestration [1–3]. However, this flue gas is very corrosive at high temperatures. Recent research revealed that both Fe-based and Ni-based Cr-containing alloys with even 25 wt% Cr are not sufficient to form a protective scale in such an environment [4–7]. However, corrosion resistance could be significantly improved by alloying with Si and/or Mn [8, 9].

In addition to the gas environment, solid particles like chloride salts and coal ash are also found to be deposited on combustion equipment surfaces, where they can affect alloy corrosion [10–12]. Our recent work [8, 9] on chloride corrosion of Fe-based and Ni-based alloys in wet CO_2 at 650 °C showed clearly that chloride salts cause severe material degradation due to active oxidation, the volatilisation of metal as chlorides [13, 14].

This paper examines corrosion behaviour of ferritic alloys, austenitic, and Ni-based alloys coated with chloride salt deposits, comparing them with salt-free surfaces in wet CO_2 at 750 °C. This temperature was chosen to match the likely requirement for advanced ultra-supercritical boilers [15, 16]. The results are compared with those at 650 °C [8, 9] to analyse the temperature effect.

Materials and Experimental Procedures

Five model alloys, Fe–25Cr, Fe–25Cr–2Mn–1Si, Fe–25Cr–20Ni, Ni–25Cr, and Ni–25Cr–2Mn–1Si (all nominal compositions in wt%) and a commercial alloy 310SS (Ni 17.7 wt%, Cr 26.1 wt%, Mn 1.4 wt%, Si 0.7 wt% analysed by the energy-dispersive X-ray spectroscopy (EDS)) were investigated. The model alloys were prepared by arc melting pure metals Fe (99.98%), Cr (99.995%), Ni (99.95%), Mn (99.9%), and Si (99.95%) under a protective Ar–5%H_2 gas atmosphere, using a non-consumable tungsten electrode. The resulting alloy buttons were annealed for 50 h at 1100 °C under flowing Ar–5%H_2 to achieve homogenisation. The 310SS alloy was supplied as a sheet and used in the as-received state without further heat treatment. Analysis by X-ray diffraction (XRD) confirmed Fe–25Cr and Fe–25Cr–2Mn–1Si to be ferritic, while the other four alloys were fully austenitic (γ-phase). Compositions of the alloys were confirmed by SEM–EDS analysis after annealing, showing only small deviations (±0.3 wt%) from the designed compositions.

The alloys were cut into approximately 9×7×2 mm rectangles and ground to a 1200-grit finish, followed by polishing to a 3-μm finish and finally electropolishing in 15% hydrochloric acid. The purpose of electropolishing was to remove the work-hardened surface zone introduced during sample preparation. Alloy grain boundaries were revealed after electropolishing [8, 9]. Alloy grains in Fe–25Cr, Fe–25Cr–2Mn–1Si, Fe–25Cr–20Ni, and Ni–25Cr were elongated, with sizes ranging from hundreds of microns to several millimetres, while the 310SS grains were much finer and more uniform, of order tens of microns.

For the gas-only experiment, sample coupons were laid on a ceramic crucible (99.5% Al_2O_3) with the upper face exposed to the gas atmosphere. This was done for comparison with the subsequent salt-deposited experiments. The ceramic crucible was placed in a horizontal alumina tube furnace for isothermal oxidation at 750 °C, and exposed to flowing gases for 300 h. The reaction gas was Ar–60%CO_2–20%H_2O (vol. %) with a linear gas flow rate of 2 cm/s at 750 °C. Argon and carbon dioxide inputs were controlled by mass flow controllers. Wet gases were generated by passing the $Ar + CO_2$ mixture through the heated water to first produce an excess amount of water vapour, which was then condensed inside a distillation column at a temperature set to achieve the required p_{H_2O} value.

For salt-deposit experiments, NaCl and KCl were dissolved in distilled water in a weight ratio of 1:1.25, in order to obtain the lowest liquidus temperature at 657 °C [9]. The solution was sprayed onto preheated specimens which were then dried using a heat gun. The coated samples were weighed after spraying, ensuring salt deposits in the range 2.5 ± 0.5 mg/cm^2. Sample coupons were laid on a ceramic crucible with coated face exposed to the flowing reaction gas. Coated alloy samples were exposed in the same way as described above for non-coated specimens, for a reaction time of 300 h. In the presence of chlorides (NaCl + KCl), the calculated equilibrium gas partial pressures [17] including p_{NaCl} and p_{KCl} and a_C are listed in Table 1.

Reacted sample surfaces were analysed by X-ray diffraction (XRD; PANalytical Empyrean with Co Kα radiation). All samples were then cold-mounted in epoxy resin for metallographic preparation. The salt deposited specimens were prepared using an oil-based lubricant to protect any remaining chlorides. Cross sections were observed and analysed by a series of techniques – optical microscopy (OM); Raman microscopy (Renishaw inVia Raman Microscope; wavelength 532 nm with argon laser); field emission scanning electron microscopy (FEI Nova NanoSEM 450) and energy-dispersive X-ray spectroscopy (EDS; Bruker); and transmission electron microscopy (TEM: Philips CM200). Samples for TEM were prepared by focused ion beam (FIB: FEI Nova Nanolab 200) milling with an accelerating voltage of 30 kV.

Table 1 Equilibrium minority gas partial pressures (atm) and a_C at 750 °C, 1 atm

Species	Ar–60CO_2–20H_2O	Ar–60CO_2–20H_2O + NaCl + KCl
O_2	1.4×10^{-7}	1.4×10^{-7}
HCl	–	1.3×10^{-5}
Cl_2	–	1.0×10^{-13}
a_c	2.5×10^{-14}	2.5×10^{-14}
NaCl	–	9.3×10^{-5}
KCl	–	1.2×10^{-4}

Results

Gas-Only Condition

Figure 1 shows metallographic cross sections of all alloys after 300 h exposure in wet CO_2 gas. For Fe–25Cr alloy (Fig. 1a), a very thin protective oxide scale was formed, identified as Cr_2O_3 in [18]. Protective behaviour was also found for Fe–25Cr–2Mn–1Si (Fig. 1b). Analysis by TEM-EDS mapping of this thin layer produced the results shown in Fig. 2. From the TEM bright field image shows the oxide scale to consist of coarse-grained outer and fine-grained inner layers. As seen from the EDS analysis and phase identifications published previously [18], the scale consists of an outer Mn-rich oxide layer, an intermediate $MnCr_2O_4$, and an inner Cr_2O_3 layer. A thin, continuous SiO_2 layer was also found at the scale–alloy interface [18].

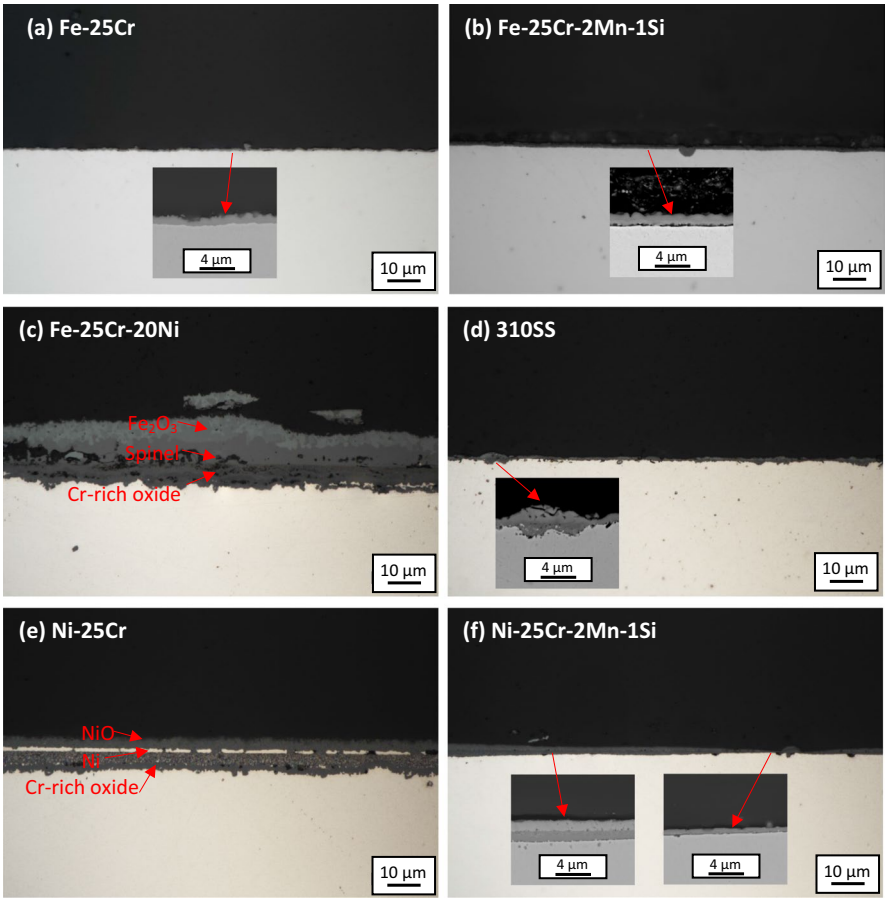

Fig. 1 Cross-sectional optical micrographs of **a** Fe–25Cr, **b** Fe–25Cr–2Mn–1Si, **c** Fe–25Cr–20Ni, **d** 310SS, **e** Ni–25Cr, and **f** Ni–25Cr–2Mn–1Si after 300 h reaction in Ar–$60CO_2$–$20H_2O$ at 750 °C

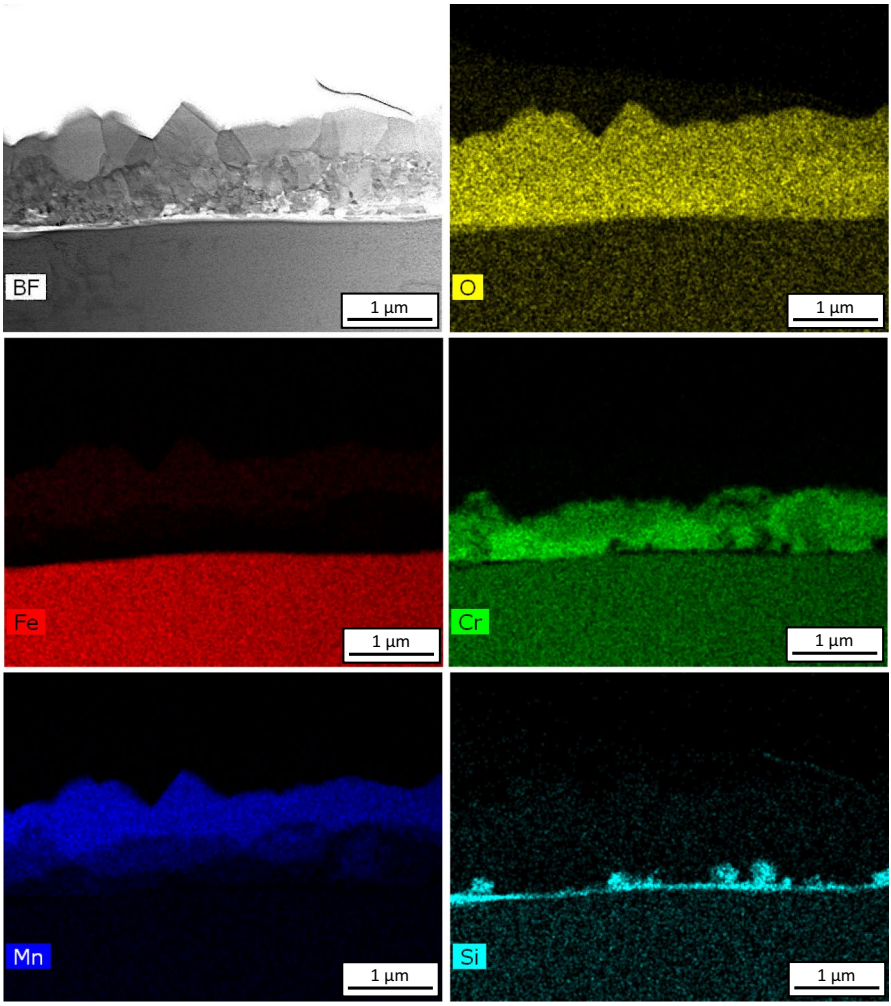

Fig. 2 TEM-EDS elemental mapping analysis of the cross section of Fe–25Cr–2Mn–1Si after 300 h reaction in Ar–60CO_2–20H_2O at 750 °C

The Fe–25Cr–20Ni austenitic alloy formed a thick multilayered scale (Fig. 1c), consisting of external Fe_2O_3, intermediate spinel, and inner chromium rich oxides [18]. While for 310SS, a protective oxide scale interrupted by small, local Fe-rich oxide nodules was observed (Fig. 1d). The TEM-EDS mapping results for the protective scale on 310SS (Fig. 3) revealed an outermost $MnCr_2O_4$ layer with Cr_2O_3 below it, and discrete islands of SiO_2 at the oxidation front [18].

A multilayered scale formed on Ni–25Cr (Fig. 1e), incorporating a metallic Ni layer within the oxide [19]. For Ni–25Cr–2Mn–1Si, a much thinner oxide was observed, and no Ni layer appeared (Fig. 1f). High magnification image revealed that this thin multilayered scale contains an outer NiO layer, a middle thin Mn-rich

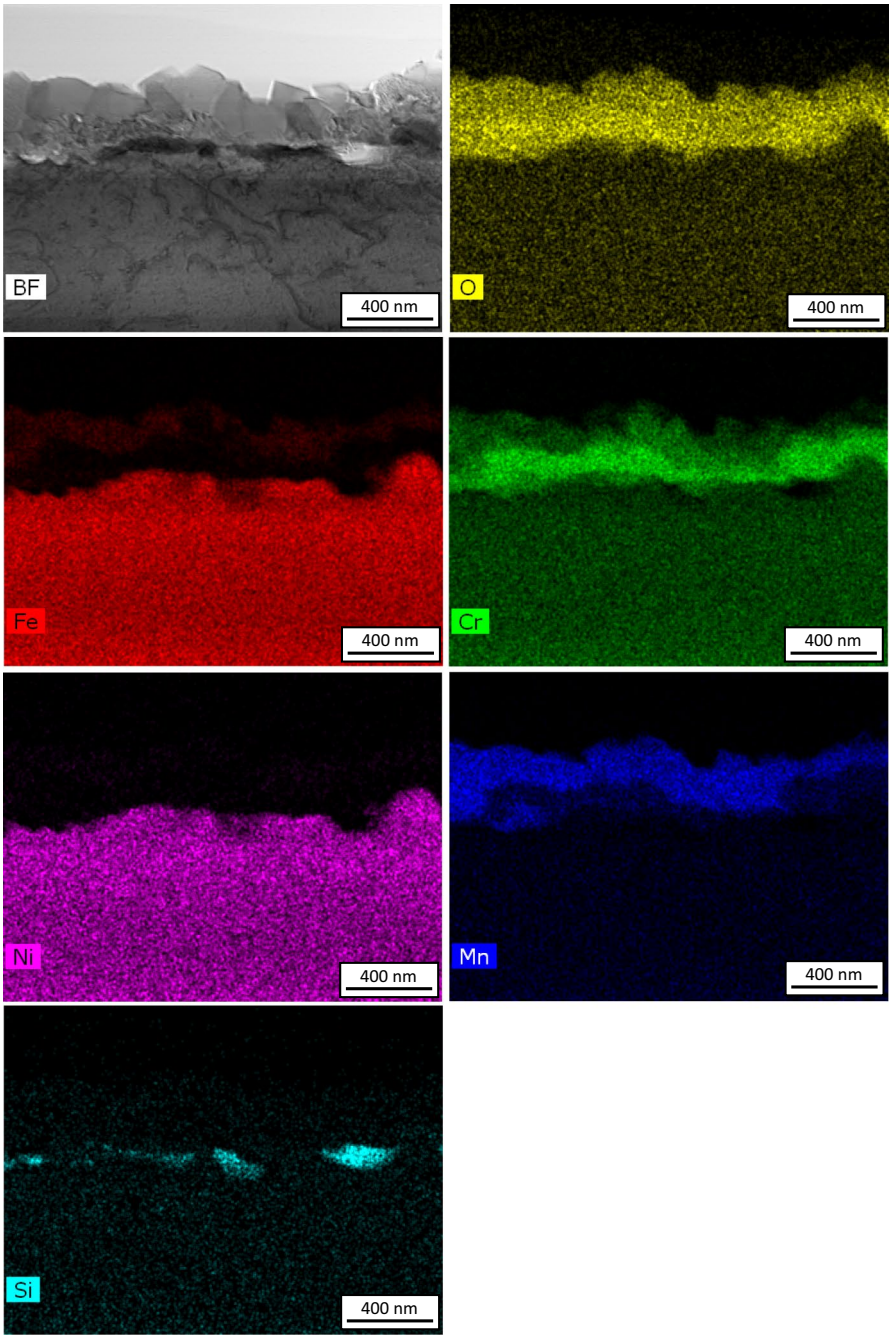

Fig. 3 TEM-EDS elemental mapping analysis of the cross section of 310SS after 300 h reaction in Ar–60CO_2–20H_2O at 750 °C

oxide layer, and an inner (Cr, Mn)-rich oxide layer (Fig. 4). There were silica precipitates at the reaction front (Fig. 4). In addition to this structure, a thin protective layer was also found to be mainly a chromia layer with a small amount of Mn_3O_4/$MnCr_2O_4$ at its surface and a silica sublayer beneath, occupying about 10% of the whole alloy surface [19].

Salt Affected Corrosion

Fe–25Cr

Metallographic cross sections of reacted Fe–25Cr after 300 h exposure are illustrated in Fig. 5. Two different structures could be observed on the surface as

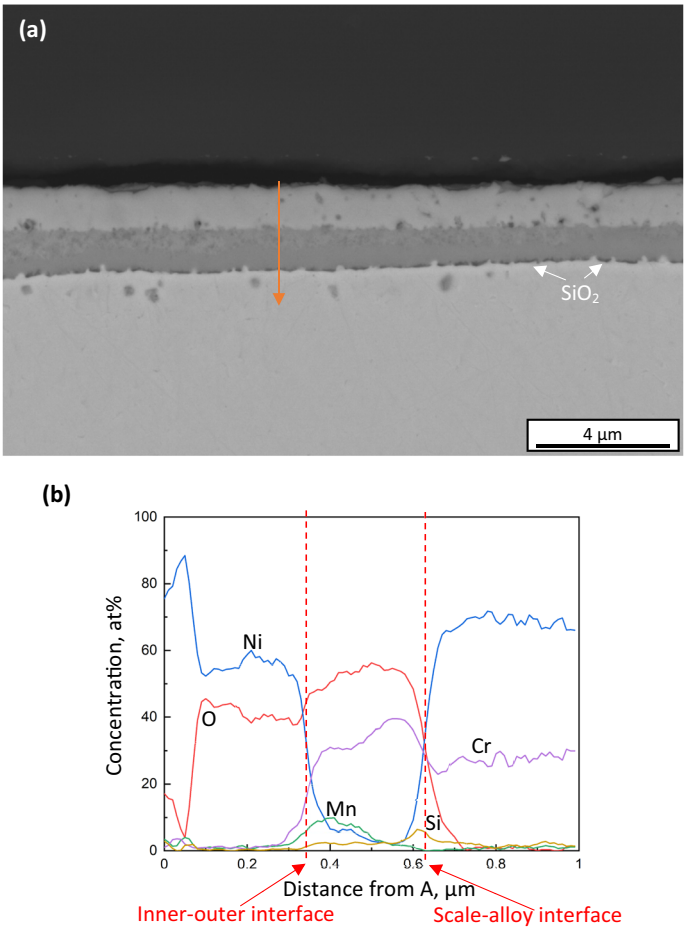

Fig. 4 **a** BSE-SEM cross section and **b** EDS-line analysis of Ni–25Cr–2Mn–1Si after 300 h reaction in Ar–$60CO_2$–$20H_2O$ at 750 °C

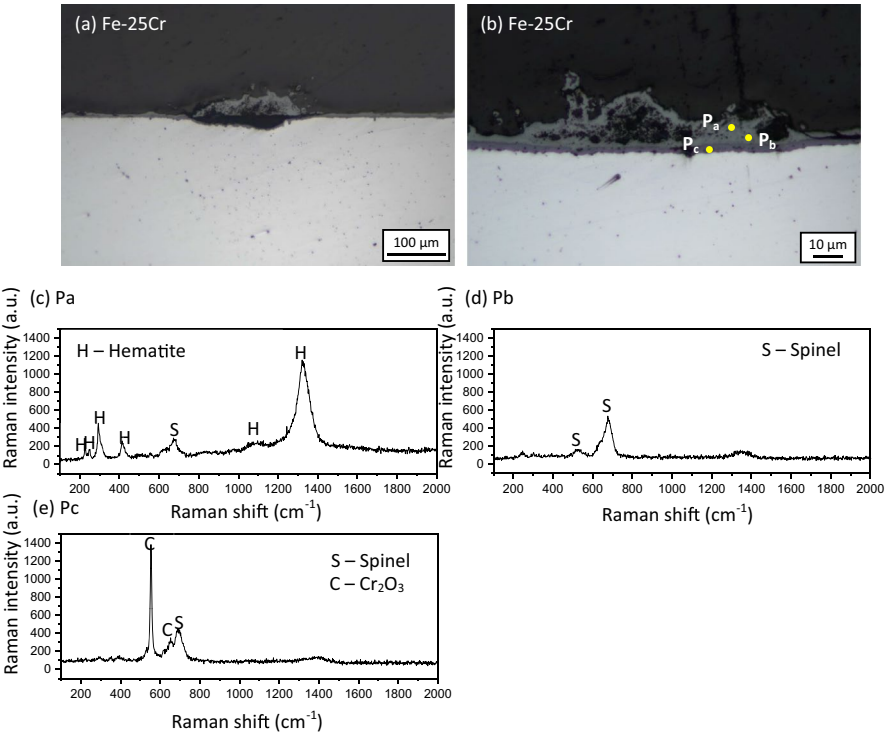

Fig. 5 **a**, **b** Cross section of Fe–25Cr after 300 h reaction beneath chloride deposits with different magnifications, and **c–e** Raman analysis results for points Pa, Pb, and Pc marked in (**b**)

shown in Fig. 5a. Oxide nodules were observed on an otherwise thin, protective oxide scale (Fig. 5a). Further analysis of the nodule (Fig. 5b) by Raman spectroscopy (Fig. 5c–e) revealed an outermost porous Fe_2O_3 layer (P_a in Fig. 5b), an intermediate spinel (P_b in Fig. 5b), and a chromia band (P_c in Fig. 5b) at the reaction front. This nodule structure was also analysed by SEM–EDS (Fig. 6a) and found to consist of porous iron-rich oxides in the thick outer oxide layer (P1 and P2 in Fig. 6a) and a thin, dense, Cr-rich inner oxide layer (P3 in Fig. 6a). It should be mentioned that quantitative element analysis by SEM–EDS is unsuccessful for light elements, and the EDS analysis of oxygen is only qualitative. Clearly there is some Cr detected inside the outer Fe-rich oxide layer (P2 in Fig. 6a). No obvious salt elements (Na, K, and Cl) were detected.

Away from the nodules, a thin oxide scale was found on the alloy (different location) to be composed of two layers as shown in Fig. 5b. Analysis of this structure by SEM–EDS mapping revealed an outer Fe-rich oxide layer above a Cr-rich layer (Fig. 6b). This structure occupied 80% of the whole alloy surface.

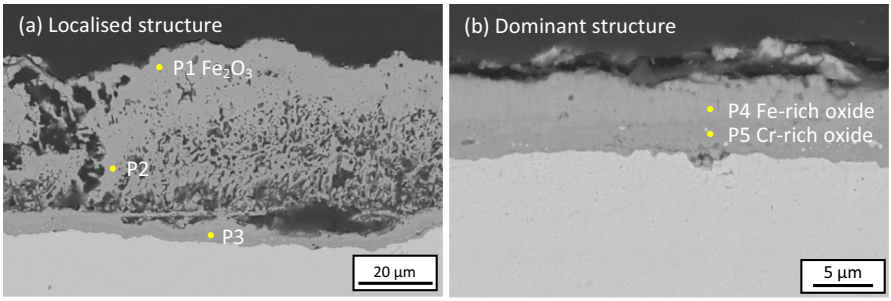

Point (at%)	Fe	Cr	O
1	48.4	0.6	51.0
2	44.9	3.6	51.5
3	5.2	41.3	53.5
4	47.6	1.5	50.8
5	6.3	42.1	51.6

Fig. 6 BSE-SEM cross section of the **a** localised structure and **b** dominant structure of Fe–25Cr after 300 h reaction beneath chlorides deposit in Ar–60CO_2–20H_2O at 750 °C

Fe–25Cr–2Mn–1Si

The scale developed on Fe–25Cr–2Mn–1Si (Fig. 7a) was ~ 7 µm thicker than that on Fe–25Cr (Fig. 5a). Mixed oxides with different contrast are seen in Fig. 7b, which mainly consist of Fe_2O_3 (P_a in Fig. 7b) and Cr_2O_3 (P_b in Fig. 7b), with an inner oxide, most likely spinel and chromia (P_d in Fig. 7b) mixed with a small amount of Fe_2O_3 (P_c in Fig. 7b). The area mapping in Fig. 8 reveals that the light contrast oxide is Fe-rich; some Cr is located in the oxide outside the original alloy surface; the inner oxide layer is enriched with Mn; and Si is located at the reaction front. Of note, Si is also enriched at the scale surface (Fig. 8). No signal for K, Na, or Cl was detected. Clearly both external and inner oxide layers are very porous with significant local scale damage. Moreover, the depletion of Fe and the enrichment of Cr confirmed the grey-shaded elongated precipitates below the scale–alloy interface to be Cr-rich carbides, as no oxygen enrichment was detected.

Fe–25Cr–20Ni

Images of Fe–25Cr–20Ni after salt affected reaction (Fig. 9a, b) show the whole surface was covered by a multilayered scale with localised deep inner oxide protrusions, as shown in Fig. 9b. According to the Raman results, Fe_2O_3 is located at

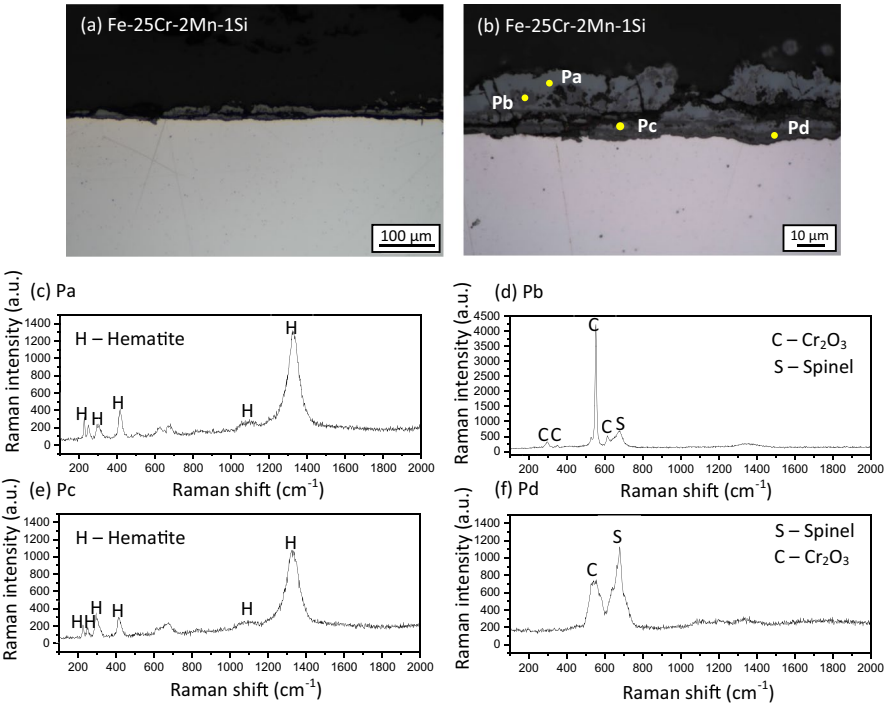

Fig. 7 **a, b** Cross section of Fe–25Cr–2Mn–1Si after 300 h reaction beneath chloride deposits with different magnifications, and **c–f** Raman analysis results for points P_a, P_b, P_c, and P_d marked in (**b**)

the external surface (P_a in Fig. 9b), with Cr_2O_3 (P_b in Fig. 9b) mixed with spinel (P_c in Fig. 9b) below the outer Fe_2O_3 layer, while an inner layer of mainly spinel (P_d and P_e in Fig. 9b) was observed, with a chromia band (P_f in Fig. 9b) at the scale–alloy interface.

An enlarged SEM view of Fig. 9b confirms that the external scale consists of Fe-rich oxides (P1 in Fig. 10), (Fe, Ni)-rich oxide (P2 in Fig. 10), and dark contrast Cr_2O_3 (P3 in Fig. 10). The pitting area contains an IOZ (internal oxidation zone) consisting of large $(Fe, Cr, Ni)_3O_4$ spinel (P4 in Fig. 10) and Ni metal (P5 in Fig. 10) particles. A thick, dense chromia band (P6 in Fig. 10) is located at the interface between the alloy and the oxides.

310SS Compared with Fe–25Cr–20Ni (Fig. 9b), 310SS (Fig. 11b) formed an even thicker scale. The thickness of its internal layer is still irregular, but more uniformly distributed over the whole surface. Dark precipitates were observed inside the metal ahead of the inner oxides. Different contrast phases visible in the external scale were Fe_2O_3 (P_a in Fig. 11b), spinel (P_b and P_c in Fig. 11b), and Cr_2O_3 (P_b and P_d in Fig. 11b). A small amount of spinel mixed with Cr_2O_3 (P_e in Fig. 11b) is located in the IOZ. SEM–EDS mapping of the outer layer (Fig. 12) revealed that the light shaded oxide is Fe-rich, while the dark contrast oxide is Cr_2O_3. An IOZ

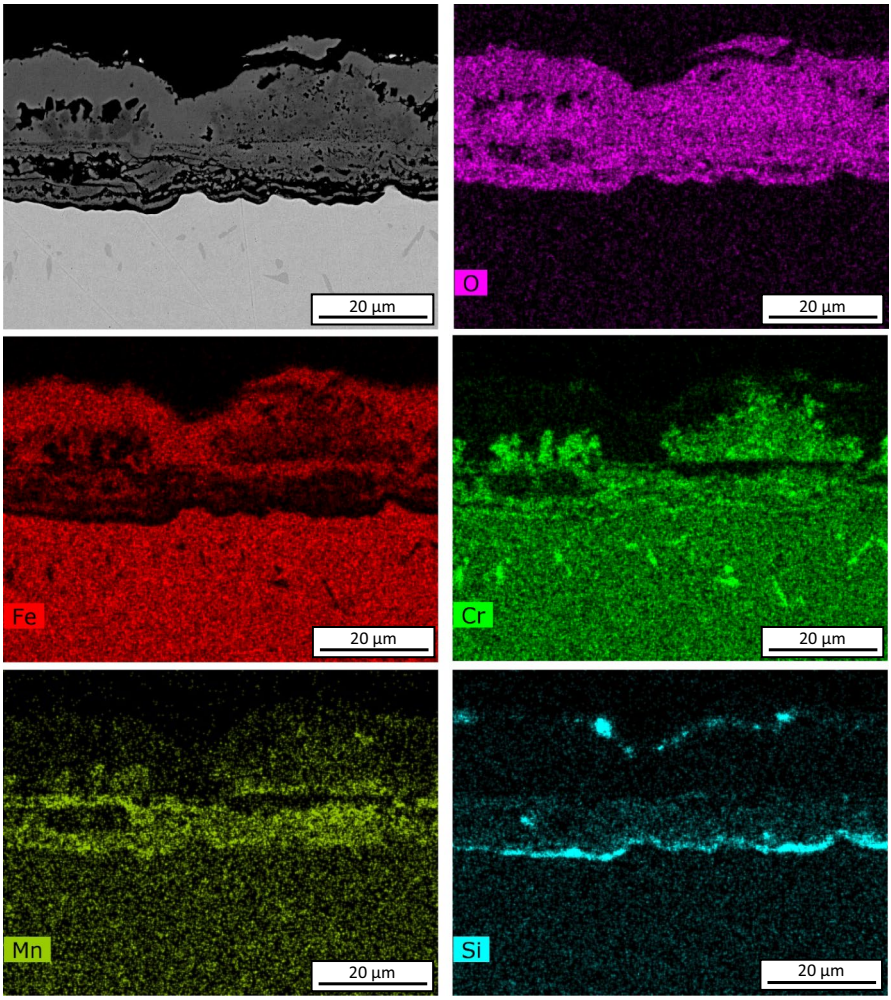

Fig. 8 BSE-SEM cross section and EDS mapping of Fe–25Cr–2Mn–1Si after 300 h reaction beneath chlorides deposit in Ar–60CO_2–20H_2O at 750 °C

was found where the metal and spinel particles are finer than the ones observed on Fe–25Cr–20Ni. In addition, silicon enrichment was seen in the black precipitate area ahead of the main reaction front. Oxide at the main reaction front was rich in Cr (Fig. 12).

Ni–25Cr

Metallographic cross sections of Ni–25Cr after 300 h exposure (Fig. 13a, c) revealed two different reaction morphologies. The first structure is shown in

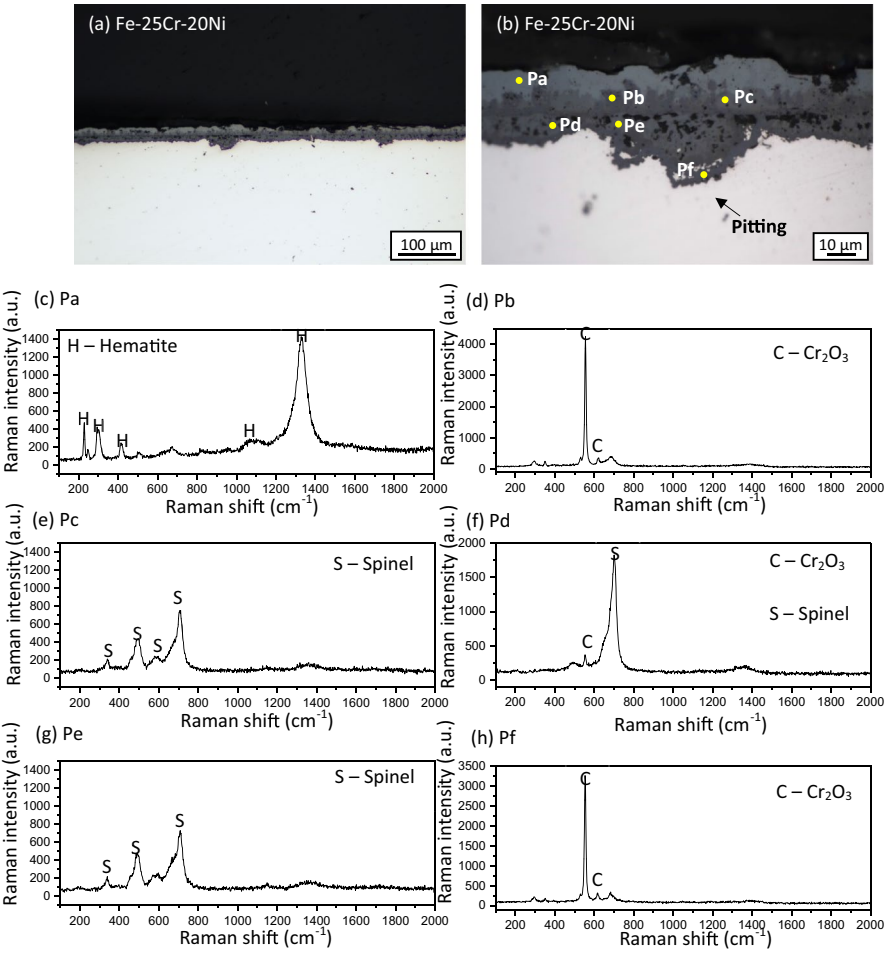

Fig. 9 **a**, **b** Cross section of Fe–25Cr–20Ni after 300 h reaction beneath chloride deposits with different magnifications, and **c**–**h** Raman analysis results for points P_a, P_b, P_c, P_d, P_e, and P_f marked in (**b**)

Fig. 13a, which is a multilayered scale. Further analysis of this structure by SEM–EDS point analysis (Fig. 13b) identifies the outer layer as NiO, located on top of the original alloy surface. In addition, an IOZ composed of (Ni, Cr) spinel and metallic Ni was found below the surface, with a Cr_2O_3 band at the reaction front.

The other structure (Fig. 13c) was found by SEM–EDS point analysis to be largely made up of a thick Cr_2O_3 layer (P5 in Fig. 13d) which is porous. An internal oxidation zone also formed, with metallic Ni particles embedded in the chromia layer (P6 in Fig. 13d). The spalled outermost thin layer contains Ni (P4 in Fig. 13d). This structure covers about 60% of the alloy surface.

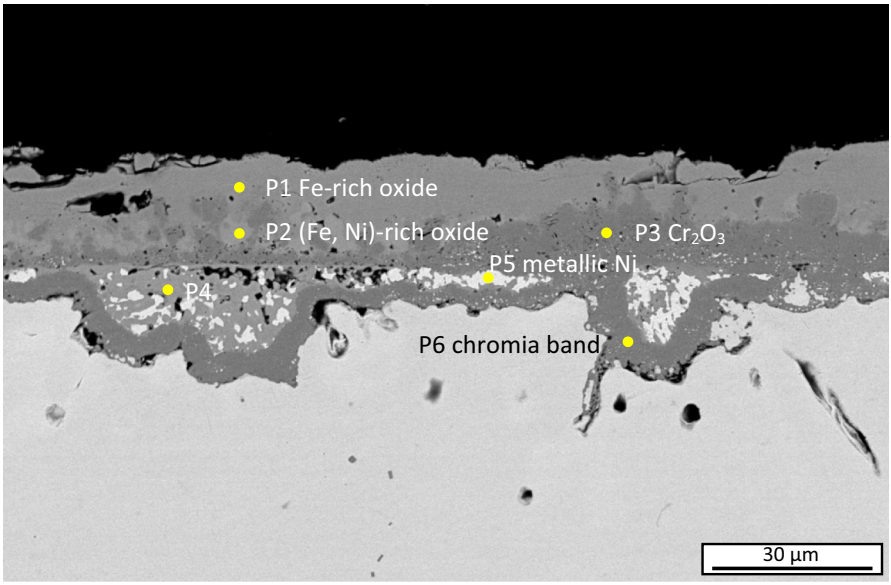

Point (at%)	Fe	Cr	Ni	O
1	49.1	1.0	-	50.0
2	36.8	1.8	15.0	46.4
3	1.5	46.3	-	52.2
4	28.5	10.7	14.8	46.0
5	8.5	2.9	86.0	2.6
6	-	47.0	-	53.0

Fig. 10 BSE-SEM cross section of Fe–25Cr–20Ni after 300 h reaction beneath chlorides deposit in Ar–$60CO_2$–$20H_2O$ at 750 °C

Ni–25Cr–2Mn–1Si

The oxide formed on Ni–25Cr–2Mn–1Si after 300h reaction (Fig. 14a, c) is thinner than that for Ni–25Cr (Fig. 13a, c), but also with two different structures. The enlarged SEM image and EDS analysis (Fig. 14b) from the location of Fig. 14a show that it consists of an external NiO scale, an IOZ containing (Cr, Mn, Si)-rich

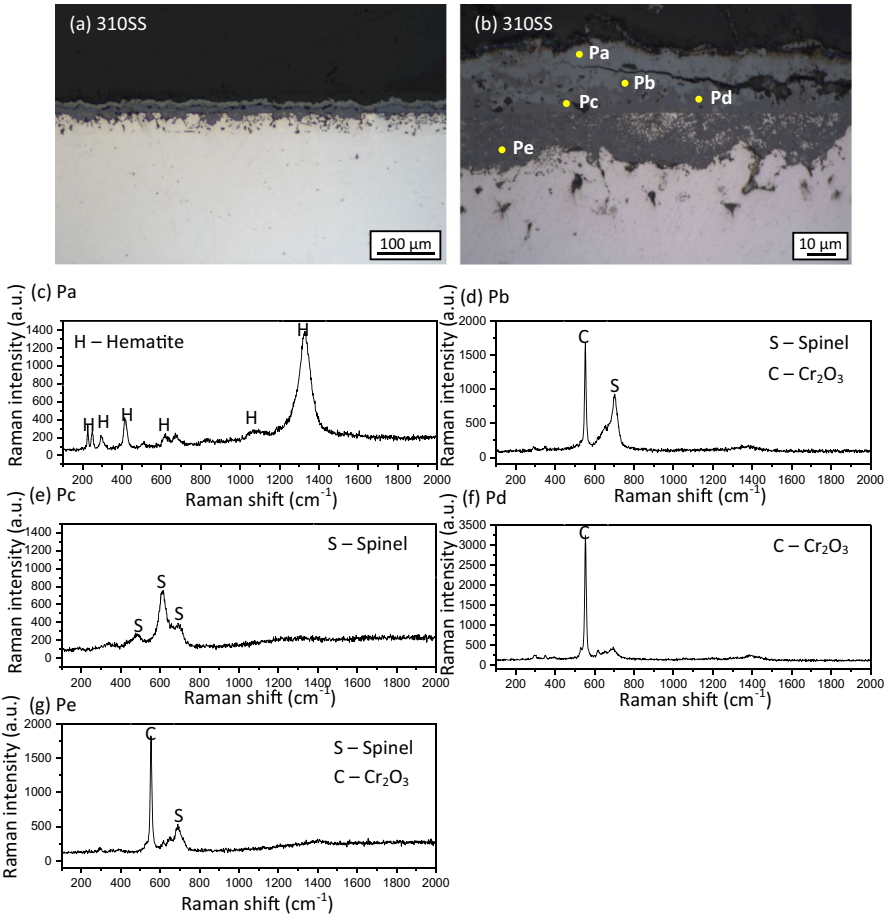

Fig. 11 **a**, **b** Cross section of 310SS after 300 h reaction beneath chloride deposits with different magnifications, and **c–g** Raman analysis results for points P_a, P_b, P_c, P_d, and P_e marked in (**b**)

oxide and a continuous (Cr, Si)-rich oxide band. A thin, semi-continuous silica layer at the reaction front was also formed.

In addition to the above typical structure, another localised structure (about 10% of the alloy surface) (Fig. 14c) was found with external Cr-rich oxide (P4 in Fig. 14d), containing dispersed nickel-rich particles in its inner region. Some voids containing silicon (P5, P6 and P7 in Fig. 14d) were located internally, and chlorine (4.6 wt%) was detected in one of them (P7 in Fig. 14d). No signal for K and Na was detected.

Carburisation

Reacted alloy cross sections were etched with Murakami's reagent to reveal the carbides formed in the alloys. Under the gas-only condition, all four iron-based

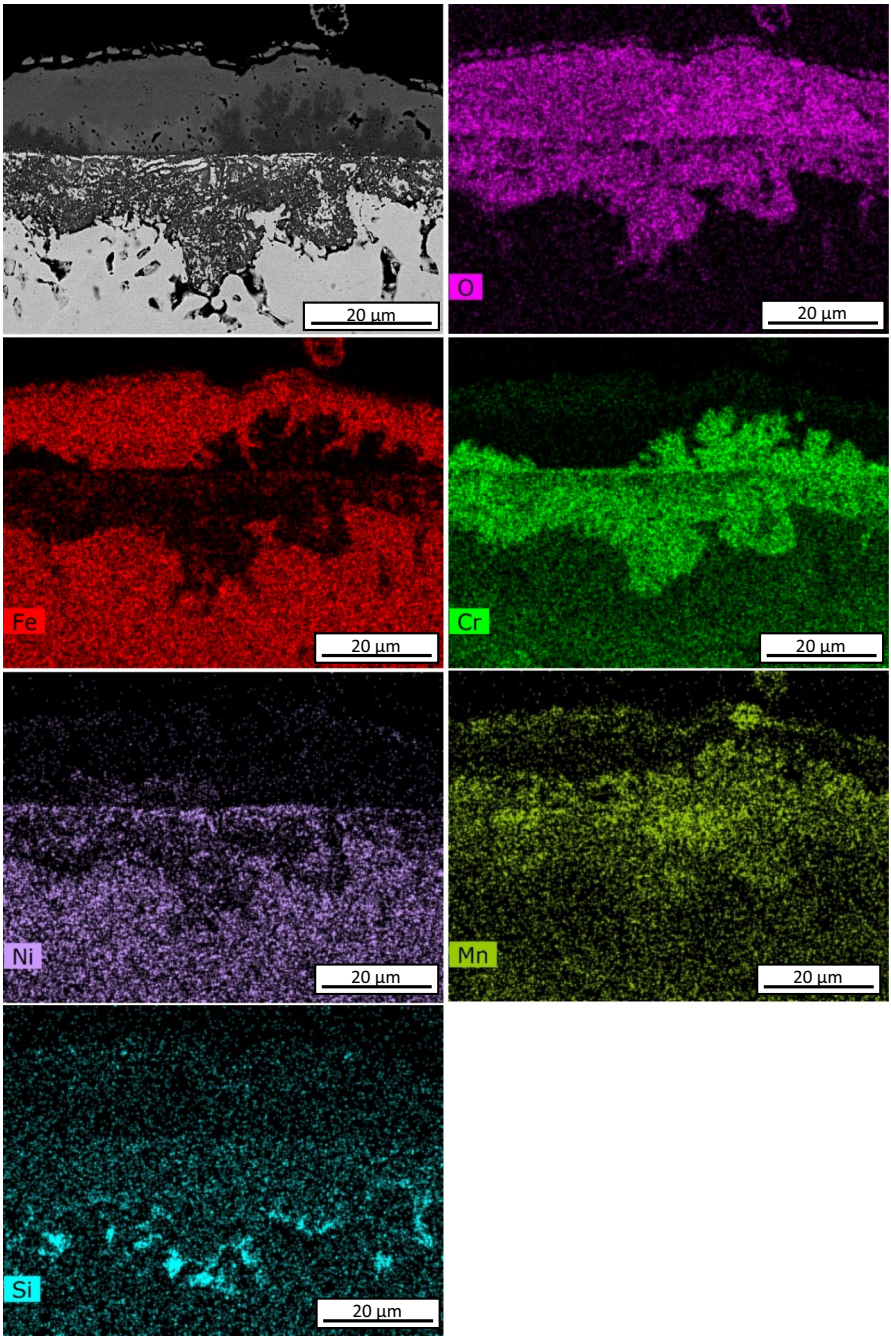

Fig. 12 BSE-SEM cross section and EDS mapping of 310SS after 300 h reaction beneath chlorides deposit in Ar–60CO_2–20H_2O at 750 °C

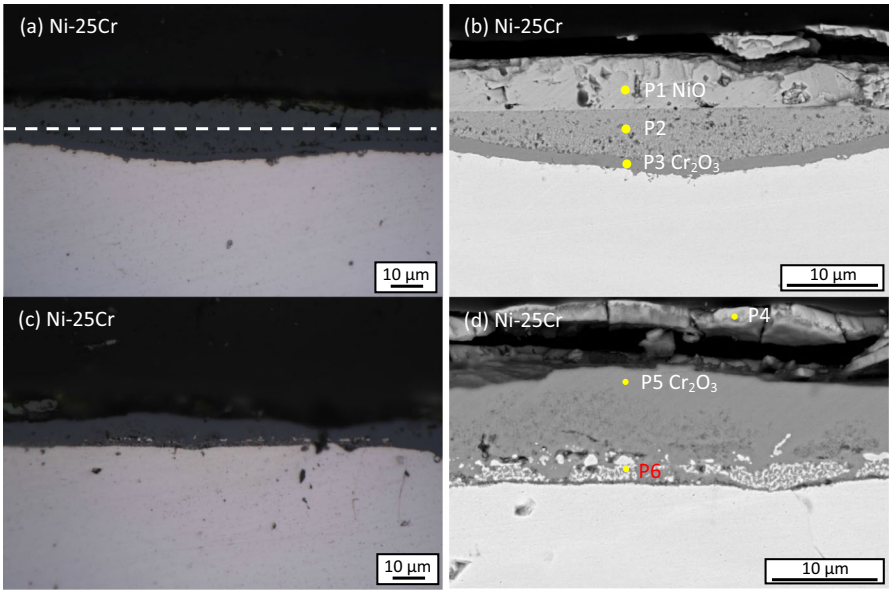

Point (at%)	Ni	Cr	O
1	49.4	1.3	49.3
2	30.2	36.5	33.3
3	2.7	36.0	61.3
4	37.1	20.4	42.5
5	0.2	43.6	56.2
6	39.6	31.1	29.3

Fig. 13 Cross-sectional optical micrographs (**a**, **c**) and BSE-SEM cross section (**b**, **d**) of Ni–25Cr after 300 h reaction beneath chlorides deposit with different structures at 750 °C, the white dashed line in **a** denotes the original surface of alloy

alloys experienced very limited carburisation by forming intergranular carbides (Figs. 15a–d). However, almost no carbides can be identified for the two Ni-based alloys under optical microscope (Figs. 15e, f). The more densely distributed carbides seen in 310SS were due to the pre-existing carbon in the unreacted material [8].

After reaction under chloride deposits, the density of the intergranular carbides in Fe–25Cr, Fe–25Cr–2Mn–1Si and Fe–25Cr–20Ni was increased considerably compared with the gas-only case. Moreover, even intragranular carbides could be observed in the sub-surface regions of Fe–25Cr (Fig. 16a) and Fe–25Cr–2Mn–1Si (Fig. 16b). Carburisation of Ni-based alloys was still negligible, with the presence of salt having little effect. Because of the presence of pre-existing carbides, any variation in carburisation extent of 310SS under the two different conditions

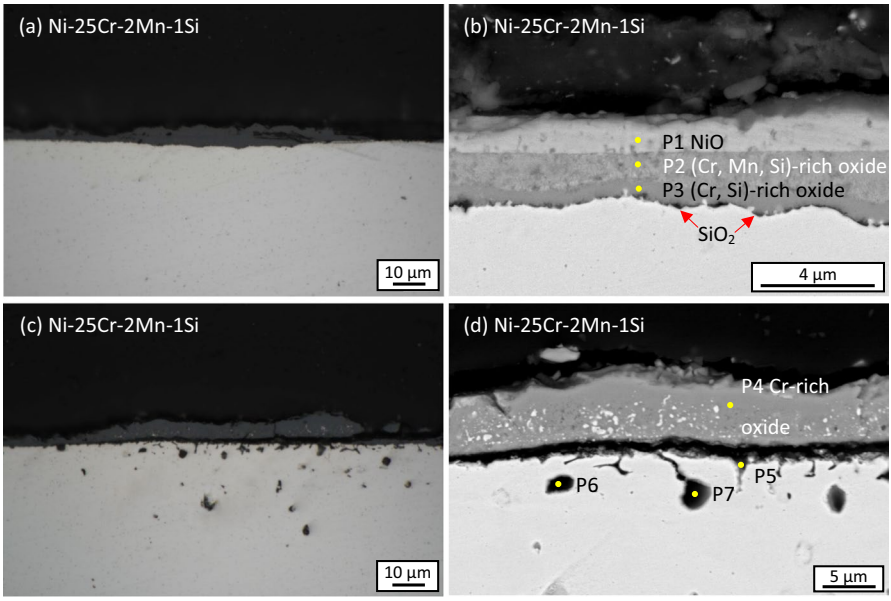

Point (at%)	Ni	Cr	Mn	Si	O	Cl
1	57.1	1.9	-	-	41.0	-
2	20.5	26.5	1.5	2.1	49.4	-
3	4.9	39.3	-	3.8	52.0	-
4	2.5	38.7	3.6	0.9	54.2	-
5	23.6	33.7	-	10.0	32.7	-
6	56.6	15.7	-	15.8	11.9	-
7	52.8	20.0	-	6.0	16.6	4.6

Fig. 14 Cross-sectional optical micrographs (**a**, **c**) and BSE-SEM cross section (**b**, **d**) of Ni–25Cr–2Mn–1Si after 300 h reaction beneath chlorides deposit with different structures at 750 °C

is hard to determine. However, some intragranular carbides formed underneath the inner oxides (Fig. 16d), indicating a degree of enhanced carbide formation.

Discussion

The corrosion behaviour of all these alloys at 650 °C has been reported [8, 9] and is compared with that at 750 °C in Table 2. The performance of austenitic and Ni-based alloys after reaction in the absence of salt is similar at the two different temperatures, but ferritic Fe–25Cr behaved differently, protective at 750 °C, but

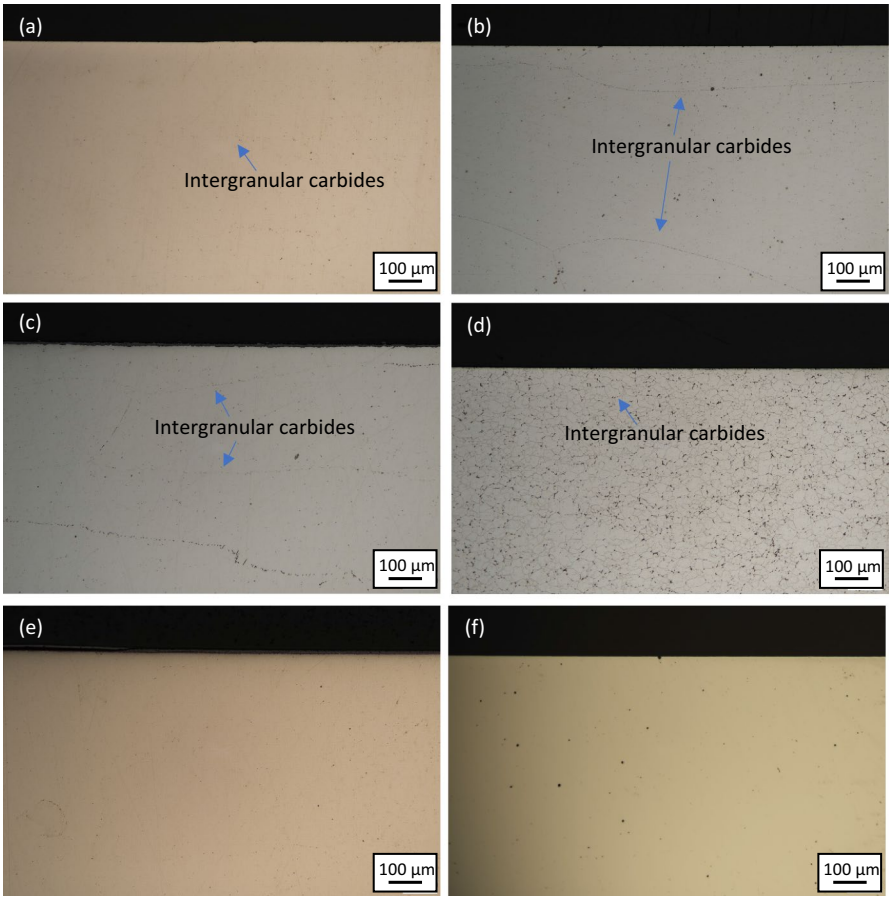

Fig. 15 Carbides formed in **a** Fe–25Cr, **b** Fe–25Cr–2Mn–1Si, **c** Fe–25Cr–20Ni, **d** 310SS, **e** Ni–25Cr, and **f** Ni–25Cr–2Mn–1Si after 300 h reaction in Ar–60CO_2–20H_2O at 750 °C

non-protective at 650 °C. Adding Mn and Si increased corrosion resistance of all three types of alloys in the gas only condition at both temperatures. However, in the presence of chloride deposits, this beneficial effect did not exist and breakaway corrosion occurred (Table 2).

The thicknesses of oxide scales for all six alloys after reactions with and without chloride deposits at 750 °C are compared in Table 3 where each thickness was determined by five measurements. Without chlorides, the additional Mn and Si significantly reduced the scale thicknesses of Fe–25Cr–20Ni and Ni–25Cr alloys. This alloying effect was not apparent for Fe–25Cr ferritic alloy which in any case performed protectively at this reaction temperature. In comparing the behaviour of 310SS with Fe–25Cr–20Ni, it is recognised that the fine-grained microstructure of the steel is another factor behind its better performance.

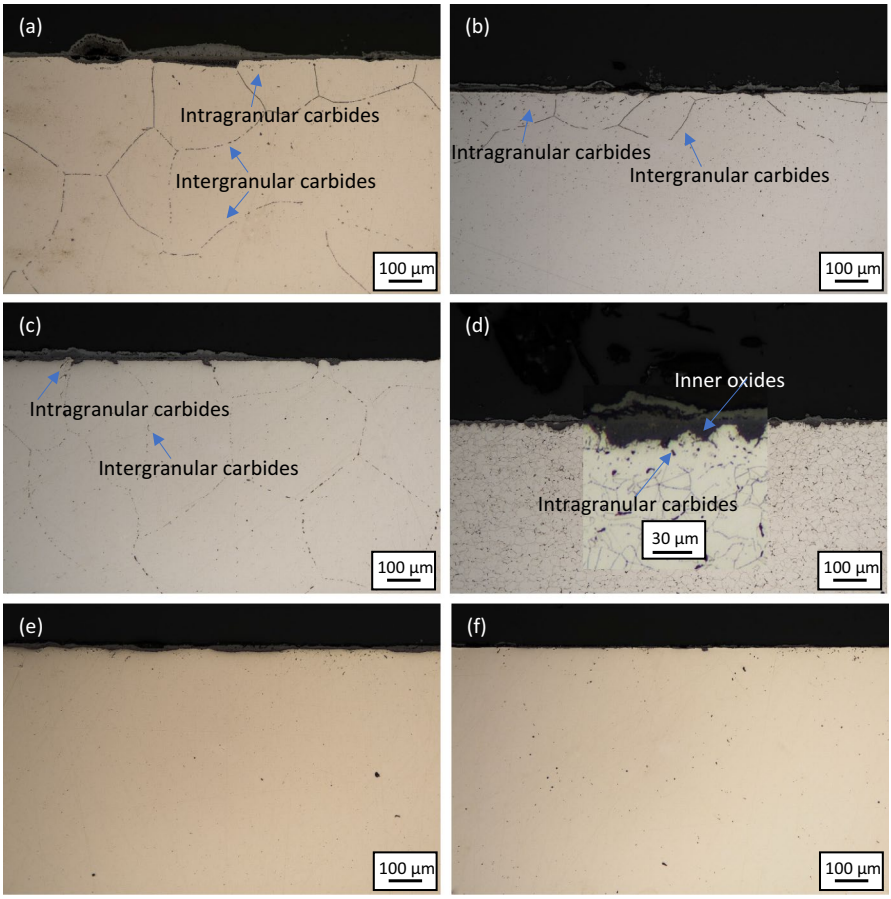

Fig. 16 Carbides formed in **a** Fe–25Cr, **b** Fe–25Cr–2Mn–1Si, **c** Fe–25Cr–20Ni, **d** 310SS, **e** Ni–25Cr, and **f** Ni–25Cr–2Mn–1Si after 300 h reaction covered by chloride deposits at 750 °C

Table 2 Summarised corrosion behaviour of all alloys at 650 °C [8, 9] and 750 °C

	Gas only		With chloride deposits	
	650 °C	750 °C	650 °C	750 °C
Fe–25Cr	Non-protective	Protective	Non-protective	Partially protective
Fe–25Cr–2Mn–1Si	Protective	Protective	Non-protective	Non-protective
Fe–25Cr–20Ni	Non-protective	Non-protective	Non-protective	Non-protective
310SS	Protective	Protective	Non-protective	Non-protective
Ni–25Cr	Non-protective	Non-protective	Non-protective	Non-protective
Ni–25Cr–2Mn–1Si	Protective	Protective	Non-protective	Non-protective

Table 3 Corrosion product thicknesses (μm) after 300 h in Ar–60CO_2–20H_2O at 750 °C

Alloys	Gas only			With chloride deposits		
	Outer scale	Inner scale	IOZ	Outer scale	Inner scale	IOZ
Fe–25Cr	~1	–	–	~2 (localised 13 ± 6)	~2	–
Fe–25Cr–2Mn–1Si	1.2 ± 0.3	–	–	11 ± 4	10 ± 3	–
Fe–25Cr–20Ni	13 ± 3	6 ± 2	–	17 ± 2	–	16 ± 9
310SS	~0.4	–	–	21 ± 4	–	18 ± 8
Ni–25Cr	3.5	–	5 ± 2	5 ± 1	–	6 ± 2
Ni–25Cr–2Mn–1Si	2	2	–	4 ± 1	–	~0.6

In the presence of chloride deposits, the pattern of alloy effects on corrosion resistance at 750 °C is rather different. Adding Mn + Si to Fe–25Cr is worse than ineffectual, leading to a substantial increase in scale thickness. Comparing the two austenitics, 310SS and Fe–25Cr–20Ni, one sees somewhat worse performance for the steel, with a slightly thicker scale and a more uniformly attacked internal zone (Figs. 9 and 11). In contrast, the presence of Mn + Si in the Ni-base alloy leads to some improvement, particularly in largely suppressing internal oxidation. Only 10% of the alloy surface underwent the internal attack, developing voids and precipitates.

Oxide scale morphologies formed on the three alloys without Mn or Si are different under the gas-only condition. Unlike its failure at 650 °C [8, 9], Fe–25Cr (Fig. 1a) formed a protective chromia layer at 750 °C. Both Fe–25Cr–20Ni (Fig. 1c) and Ni–25Cr formed an IOZ with a multilayered outer scale for the former, and an expelled Ni layer overgrown by a continuous NiO layer for the latter. After adding Mn and Si to the alloys, all three alloys behaved protectively with a thin dense protective scale formed.

When reacted under chloride deposits, all alloys experienced more extensive corrosion than those in the gas only condition. Similar to what was reported for 650 °C, more porous oxides were observed and significant relocation of Cr from the metal substrate to the external oxide scale was identified for both ferritic and austenitic iron-based alloys. However, for the two Ni-based alloys (Figs. 13a, c, 14a, c), porosity within the oxide scales is very small. Localised alloy porosity was found at the reaction front for both austenitic iron-based alloys (Fig. 10) and Ni-based alloys (Figs. 13a, c, 14a, c).

The oxidation performance of alloys in the gas-only condition is first reviewed and compared with that at 650 °C. Effects of chloride salt deposits and the temperature effect in the presence of chlorides are then examined.

Corrosion of Alloys Under Gas-Only Condition

To understand the different corrosion behaviour of alloys in the gas-only condition at 650 °C [9] and 750 °C, the critical Cr concentrations for protective chromia formation were calculated from Wagner's equations [20, 21]. Critical values are listed in Table 4 [8, 9, 18, 19]. Here, $N_{Cr}^{(1)}$ is the critical value for external chromia

Table 4 Critical chromium concentrations $N_{Cr}^{(1)}$ and $N_{Cr}^{(2)}$ at 650 °C [8, 9] and 750 °C[18, 19]

	Fe–25Cr		Fe–25Cr–20Ni		Ni–25Cr	
	650 °C	750 °C	650 °C	750 °C	650 °C	750 °C
$N_{Cr}^{(1)}$	0.15	0.07	0.07	0.08	0.31	0.22
$N_{Cr}^{(2)}$	0.11	0.04	0.42	0.32	N/A	0.27–0.39

formation rather than its internal precipitation, and $N_{Cr}^{(2)}$ for the maintenance of continued growth of that scale.

The results indicate that the Cr concentration of the alloy is high enough for chromia formation and maintenance for Fe–25Cr, but not for Fe–25Cr–20Ni and Ni–25Cr alloys at either temperature. Comparing the critical Cr values at 650 °C and 750 °C in Table 4, there is a significant decrease in both $N_{Cr}^{(1)}$ and $N_{Cr}^{(2)}$ for Fe–25Cr with increasing temperature, due to the temperature sensitivity of alloy Cr diffusion. The prediction is in line with the observed protective oxide formation at the higher temperature. Although the calculation suggests also protective oxide formation for Fe–25Cr at 650 °C, a thick multilayered scale was grown instead. This was attributed to the formation of internal chromium carbides, leading to a substantially lowered subsurface Cr concentration [9]. Clearly, the decrease in the critical Cr concentrations at 750 °C benefits the formation of a protective oxide scale.

The beneficial effects of Si and Mn alloying are significant at both temperatures, promoting protective chromia scale formation for all alloys. These effects have been well explained by forming an additional silica sublayer or silica precipitates at the reaction front which provide a diffusion barrier effect. The rapid diffusion rate and high solubility of Mn in chromia enable the formation of Mn-bearing oxides, such as $(Cr, Mn)_2O_3$ or $(Cr, Mn)_3O_4$. These potential Mn-bearing oxides could further enhance the protective properties of the oxide scale formed during reaction [22]. These alloying effects are demonstrated by the microstructure analyses shown in [8, 9] at 650 °C and in Figs. 2, 3, and 4 at 750 °C.

The observed Mn-enriched oxide, located above the inner (Cr, Mn)-rich oxide layer (Fig. 4), could also be attributed to the higher diffusion coefficient of Mn ($\sim 10^{-17}$ cm^2/s) [23] than that of Cr in Cr_2O_3 ($\sim 10^{-30}$ cm^2/s) [24] at 750 °C. Both MnO and $MnCr_2O_4$ are stable phases, enabling Mn enrichment at the top of the inner layer [25].

Effects of Chloride Deposit

As mentioned at the beginning of the discussion, porous oxides and/or alloy subsurface pores were found at both 650 °C [8, 9] and 750 °C (Figs. 5, 6a, 7b, 9b, 10, 11b, 13b, d). This phenomenon can be explained by the so-called active oxidation mechanism [9, 26–29]. In the presence of chlorides (NaCl and KCl), Cl_2 can be produced from reaction between salt and water vapour, hence initiating the formation of metal chlorides by the reaction within and beneath the scale of metal or metal oxides with Cl_2. These metal chlorides are volatile and can transport outward to be reconverted to oxides at high p_{O_2} values near the gas–oxide interface. The Cl_2 formed from this

conversion will then react with the remaining metal oxide and this reaction cycle will be repeated, continuing active corrosion:

$$\frac{2}{x}\mathrm{M(s)} + \mathrm{Cl_2}(g) = \frac{2}{x}\mathrm{MCl}_x(s,g) \tag{1}$$

$$\mathrm{MO}_y(s) + \frac{x}{2}\mathrm{Cl_2}(g) = \mathrm{MCl}_x(g) + \frac{y}{2}\mathrm{O_2}(g) \tag{2}$$

where forward Eq. 2 represents oxide volatilisation, favoured where $p_{\mathrm{Cl_2}}$ is high, and the reverse reaction describes chloride re-oxidation and deposition externally where $p_{\mathrm{O_2}}$ is high.

As shown in Tables 2 and 3, during corrosion under a salt deposit, all alloys underwent breakaway oxidation at 650 °C, while Fe–25Cr and Ni–25Cr–2Mn–1Si exhibited partially protective behaviour at 750 °C, and all other alloys were non-protective.

A protective $\mathrm{Cr_2O_3}$ scale (Fig. 1a) was formed on Fe–25Cr under the gas-only condition at 750 °C. However, in the presence of chloride deposits, a thin double-layered scale was formed, together with local nodules of thick, porous Fe-rich oxide (Fig. 5b). In contrast, at 650 °C, thick multilayered scales formed on Fe–25Cr in both gas-only and under-deposit conditions. As discussed in Sect. 4.1, the difference is attributed to the faster diffusion of alloy Cr and the consequently enhanced ability to form chromia at 750 °C. Evidently the presence of chloride salt mitigates the improvement in corrosion resistance at the higher temperature.

To understand the conversion from the protective $\mathrm{Cr_2O_3}$ layer in the gas-only condition (Fig. 1a) to a double layer with nodules for Fe–25Cr in the presence of chloride deposits (Fig. 5b), volatilisation of $\mathrm{Cr_2O_3}$ in the presence of chlorine is considered:

$$2\,\mathrm{Cr(s)} + \frac{3}{2}\mathrm{O_2(g)} = \mathrm{Cr_2O_3(s)} \quad \Delta G^{\mathrm{o}} = -861.4\ \mathrm{kJ} \tag{3}$$

$$\mathrm{Cr_2O_3(s)} + 2\,\mathrm{Cl_2(g)} = 2\,\mathrm{CrCl_2(g)} + \frac{3}{2}\mathrm{O_2(g)} \quad \Delta G^{\mathrm{o}} = 480.0\ \mathrm{kJ} \tag{4}$$

$$\frac{1}{2}\mathrm{Cr_2O_3(s)} + \mathrm{Cl_2(g)} + \frac{1}{4}\mathrm{O_2(g)} = \mathrm{CrO_2Cl_2(g)} \quad \Delta G^{\mathrm{o}} = 35.7\ \mathrm{kJ} \tag{5}$$

where the standard free energy changes [17], ΔG^0, are evaluated at 750 °C.

At the oxide-gas interface, $p_{\mathrm{O_2}} = 1.4\times10^{-7}$ atm, and equilibrium values of $p_{\mathrm{CrCl_2}} = 7.7\times10^{-21}$ atm and $p_{\mathrm{CrO_2Cl_2}} = 2.9\times10^{-17}$ atm were calculated based on Eqs. (3–5). It is concluded on this basis that if an external protective chromia layer is able to form before $\mathrm{Cl_2}$ is produced, the volatilisation would be suppressed.

At the oxide-alloy interface, $p_{\mathrm{O_2}}$ is controlled by the local $\mathrm{Cr/Cr_2O_3}$ equilibrium. Approximating $a_{\mathrm{Cr}} \approx 0.25$, a value of $p_{\mathrm{O_2}} = 3.30\times10^{-29}$ atm is calculated. If the $p_{\mathrm{Cl_2}}$ value at the oxide-gas interface (1.0×10^{-13} atm) is used as the maximum value for the estimation, the resulting $p_{\mathrm{CrO_2Cl_2}}$ value is 1.1×10^{-22} atm, and hence,

the vaporisation of this species can be neglected. However, p_{CrCl_2} is found to be 1.4×10^{-4} atm, indicating the occurrence of appreciable vaporisation [30–32]. It is therefore concluded that if Cl_2 penetrates the chromia scale, it is likely to lead to the volatilisation of the oxide as $CrCl_2$. This results in the observed migration of Cr to the external oxide scale (Fig. 6a) and the loss of chromia protection at 750 °C. This conclusion should also apply for Fe–25Cr at 650 °C if chromia forms. However, no chromia scale formed at 650 °C, and the porous iron oxide scale formation was attributed to vaporisation of iron-rich oxides [8]. If such a process occurred at 750 °C, it would also affect the oxide scale morphology. The possibility of iron oxide volatilisation at this temperature is now considered.

Figure 17 shows the Fe–O–Cl predominance diagram at 750 °C, calculated from FactSage 8.1 [17]. A dashed line added on the Fe–O–Cl stability diagram represents the vapour pressure for $FeCl_2$ (g) of 10^{-4} atm, above which substantial volatilisation is generally assumed [30–33]. The point marked as a star labelled A on the diagram represents gas phase conditions at the scale surface and is in the Fe_2O_3 field. This oxide is therefore predicted to occur at the scale surface, as was observed. If chlorine can enter the scale and diffuse inward, the resulting diffusion path is represented schematically by the dotted line A-B. When this path intercepts the dashed line, volatilisation of $FeCl_2$ becomes significant, and oxide is consumed, leaving a porous oxide scale. Such a process accelerates porous oxide formation for Fe–25Cr, as observed in Fig. 6a.

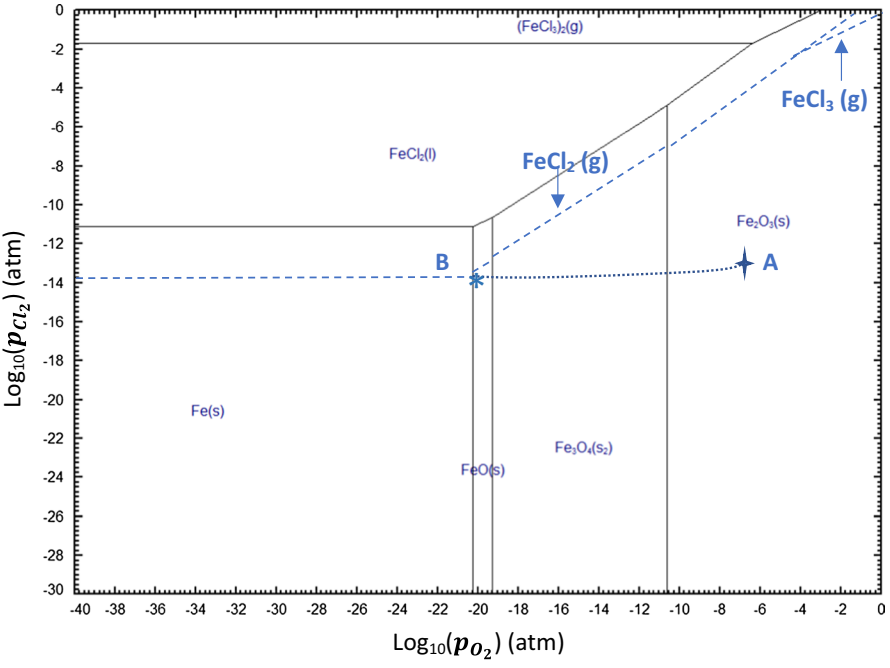

Fig. 17 Traditional stability diagram and quasi-stability diagram (dashed lines calculated for $p_{FeCl_2} = 10^{-4}$ atm) of Fe–O–Cl system at 750 °C. "Star A" represents the experimental condition, dotted line AB represents an assumed diffusion path for oxygen and chlorine from the oxide/gas to oxide/metal interface

Over the majority of the surface, however, the iron oxide layer remains intact above a Cr-rich oxide in contact with the alloy. It seems therefore, that conditions are marginal for volatilisation, and small local variations in salt deposit amounts and oxide microstructure might lead to chlorine access to the scale interior. It is noted that the thermochemical diagram in Fig. 17 is not directly applicable: no metal-FeO phase boundary forms on the alloy as Cr quickly diffuses to create a continuous $(Cr, Fe)_2O_3$ layer. The boundary of interest is between that oxide and the outer $(Fe,Cr)_2O_3$ layer. Here the iron activity is far below that of the alloy, and a higher value of p_{O_2} is in effect. Consequently, the p_{Cl_2} value required to volatilise iron oxide is higher. As long as this situation is maintained, the scale is stable and protective, as shown in Fig. 6b. However, if chlorine can reach this interface, the more easily volatilised chromia can react, as seen in Fig. 6a, triggering local loss of protection.

For the austenitic alloy, Fe–25Cr–20Ni under the chloride-covered condition, external Fe_2O_3, Cr_2O_3 and $(Fe, Cr)_3O_4$ layers were formed (Fig. 9). Moreover, an internal oxidation zone (IOZ) was detected on Fe–25Cr–20Ni (Fig. 10), due to the high concentration of Ni in the alloy. The $(Fe, Cr)_3O_4$ spinel precipitates locally within the alloys, consuming Fe and Cr while expelling Ni to form the matrix of the IOZ.

The interactions of those oxides with Cl_2 in the chloride salts at 650 °C have been assessed by calculating [8] the maximum possible partial pressures of $NiCl_2$, $FeCl_2$ and $CrCl_2$. The conclusion was that the volatilisation of $NiCl_2$ is negligible, but that of $FeCl_2$ and $CrCl_2$ is feasible. Using the same calculation, this conclusion remains unchanged for the 750 °C case where the corresponding partial pressures are: $p_{NiCl_2} = 6.9\times10^{-8}$ atm, $p_{CrCl_2} = 6.4\times10^{-4}$ atm, and $p_{FeCl_2} = 3.2\times10^{-4}$ atm, indicating possible iron and chromium volatilisation via their chlorides.

The oxides formed on Ni–25Cr under chloride salt deposits at 750 °C are similar to those formed at 650 °C. Reactions of NiO, Cr_2O_3, or spinel with chlorine gas were discussed in [8]. By using the p_{Cl_2} value at the gas–scale interface, and the p_{O_2} value from the Cr/Cr_2O_3 equilibrium (in the same way as at 650 °C [8]), it is found that $p_{NiCl_2} = 5.3\times10^{-12}$ atm, and $p_{CrCl_2} = 1.4\times10^{-4}$ atm at 750 °C. Therefore, preferential volatilisation of chromium is predicted. Evidently chlorine did reach the underside of the scale, leading to the predicted outward transport of Cr, as shown by the formation of a thick, porous, outer chromia scale layer (Fig. 13d). The observation of an additional thin spalled oxide layer containing varying concentrations of Ni on the top of the thick chromia layer (P4 and P5 in Fig. 13d) is attributed to the initial stage of oxidation.

In addition to the porous oxides formed in the presence of chlorides, a considerable amount of external Cr-bearing oxide formed on all six alloys (Figs. 6, 8, 10, 12, 13d, 14d) which is attributed to the vaporisation of chromia by chlorine. This phenomenon was found at both temperatures, but with more Cr transported outward at 750 °C. For Fe–25Cr ferritic alloy, the amount of Cr carried out was very limited at 650 °C [9], but more Cr was relocated to the external oxide scale at 750 °C (Fig. 6). For Fe–25Cr–20Ni, the outer Cr-rich oxide was localised at 650 °C [8], but became continuous although non-uniform at 750 °C (Fig. 10). For Ni–25Cr, the area of the structure with thick chromia oxide was increased from 40% at 650 °C [8] to 60% at 750 °C (Fig. 13c). Those differences are attributed to the increased partial pressure

(two to ten times the values at 650 °C) of $CrCl_2$ produced at 750 °C, which increases the rate of volatilisation.

With the presence of chloride salts (Figs. 8, 12, 14), the beneficial effects of both Mn and Si observed in the gas-only condition (Figs. 2, 3, and 4) disappeared on all alloys at 750 °C, as they did also at 650 °C. It is noteworthy that the oxide layers (Table 3) formed on Fe–25Cr–2Mn–1Si (Fig. 7b) and 310SS (Fig. 11b) are even thicker than those formed on the Si- and Mn-free alloys (Figs. 5b, 9b). An explanation can be found in the volatilisation of the additional SiO_2, Mn_3O_4, and $(Mn, Cr)_3O_4$ spinel products:

$$SiO_2(s) + 2Cl_2(g) = SiCl_4(g) + O_2(g) \quad \Delta G^o = 198.2\ kJ \tag{8}$$

$$Mn_3O_4(s) + 3Cl_2(g) = 3MnCl_2(g) + 2O_2(g) \quad \Delta G^o = 122.8\ kJ \tag{9}$$

The predicted partial pressures of $SiCl_4$ and $MnCl_2$ can be calculated, by using p_{O_2} at Cr/Cr_2O_3 equilibrium, which yields $p_{SiCl_4} = 2.3 \times 10^{-8}$ atm, and $p_{MnCl_2} \gg 1$ atm. According to the Bender et al. [32, 33], a vapour pressure of 10^{-4} atm is considered a significant level for metal consumption. Therefore, it is concluded that only Mn could be volatilised at the very low oxygen partial pressure at the Cr/Cr_2O_3 equilibrium. Moreover, the diffusion rate of Mn is fast in Cr_2O_3 [24]. These two processes explain why Mn could be detected externally. The existence of Cl at the porous region (P7 in Fig. 14d) indicates the possible formation of $SiCl_4$ locally, which explains why the protective effect of Si disappeared.

Carburisation

Comparison of the carburisation results (Figs. 15 and 16) for the gas-only and chloride-coated cases, reveals that the extent of Fe-based alloy carburisation is significantly affected by the chloride deposits. While only sparsely distributed intergranular carbides were found after gas-only reaction, some intragranular carbides were also found in the subsurface regions of Fe-based model alloys beneath chloride deposits (Fig. 16a–c).

Carbide fractions measured by ImageJ [34] in reacted 310SS seemed very similar in the two cases (gas-only: $f_v = 0.036 \pm 0.001$, and chloride-deposited: $f_v = 0.037 \pm 0.001$). This reflects the fact that most carbides are intergranular, which come from the carbon originally present in the steel. Significantly, intragranular carbides developed near the surface in the presence of chlorides (Fig. 16d). Carburisation of Ni-based alloys (Figs. 15e–f, 16e–f) was very similar after reaction without and with chloride deposits, being negligible in both cases.

The increased carburisation of Fe-based alloys when exposed under chloride deposits reflects the greater carbon permeability of the non-protective scales grown in these conditions. Just as oxidation is faster in the presence of chloride, so too is carbon ingress.

The difference in carburising behaviour between Fe-based and Ni-based alloys is due to significantly different carbon diffusion coefficients in Fe-based (ferritic and austenitic: 3.9×10^{-7} [35], 1.8×10^{-8} $cm^2\ s^{-1}$ [36], respectively) and Ni-based alloys

(6.6×10^{-9} cm^2 s^{-1} [37]). Moreover, as mentioned in Sect. 4.2, Ni metal is not prone to active oxidation because of the very low p_{NiCl_2}, which alleviates the chloride effects on oxidation and also carburisation of Ni-based alloys.

Conclusions

Fe-based Fe–25Cr, Fe–25Cr–2Mn–1Si, Fe–25Cr–20Ni, 310SS, and Ni-based Ni–25Cr, Ni–25Cr–2Mn–1Si alloys were reacted in Ar–$60CO_2$–$20H_2O$ gas without and with chloride salt deposits at 750 °C. When reacted in the gas-only condition, Fe–25Cr formed a protective chromia scale, while both Fe–20Ni–25Cr and Ni–25Cr formed multilayered oxides. The difference is due to the faster diffusion of Cr in bcc than in fcc alloys. Alloy additions of Mn and Si improved the corrosion resistance of all alloys by promoting protective silica formation at the scale–alloy interface and relatively slow-growing Mn-rich oxides rather than Fe- or Ni-rich ones.

When exposed to reaction in the presence of chloride deposits, all six alloys underwent accelerated breakaway corrosion by forming more porous oxide scales. Significant Cr relocation from the alloy to outer oxide scale regions was observed. These phenomena reflect the operation of the so-called active corrosion mechanism where volatile iron and/or chromium chlorides are formed inside the oxide scale and transport outwards to be reconverted to oxides where p_{O_2} is high. Thermodynamic analysis revealed higher partial pressures of $FeCl_2$ and $CrCl_2$ formed at 750 °C than at 650 °C, accounting for the increased amount of relocated Cr in the external oxide scale and greater oxide porosity found at 750 °C.

Faster diffusion of Cr in the Fe–25Cr alloy led to a partially protective chromia scale at 750 °C, even when chloride was present.

The protective effect of Si and Mn was not observed in the presence of chloride salt, and rather thick oxide layers were formed on Fe–25Cr–2Mn–1Si and 310SS. Thermodynamic analysis demonstrated that the volatilisation of Mn is significant, and any silica subscale is damaged by reaction with chlorine.

Only very limited intergranular carburisation was found for all Fe-based alloys and negligible carbides for Ni-based alloys in the gas-only condition. In the presence of chlorides, the two Ni-based alloys behaved similarly to the gas-only case. However, some intragranular carbides were also found in all four Fe-based alloys. This difference can be attributed to faster carbon diffusion in iron-based alloys and less accelerated attack on nickel-based alloys by chloride due to less volatile chloride formation.

Acknowledgements Financial support from the Australian Research Council Discovery Program is highly appreciated.

Author contributions YC wrote the main manuscript text and prepared the figures. ZZ analysed data and prepared figures. All authors reviewed the manuscript.

Funding Open Access funding enabled and organized by CAUL and its Member Institutions.

Declarations

Conflict of interest The authors declare that they have no conflict of interest.

References

1. C. Yin and J. Yan, *Applied Energy* **162**, 742 (2016).
2. M. A. Nemitallah, M. A. Habib, H. M. Badr, S. A. Said, A. Jamal, R. Ben-Mansour, E. M. Mokheimer, and K. Mezghani, *International Journal of Energy Research* **41**, 1670 (2017).
3. C. Liu, G. Chen, N. Sipöcz, M. Assadi, and X. S. Bai, *Applied Energy* **89**, 387 (2012).
4. C. Yu, J. Q. Zhang, and D. J. Young, *Corrosion Science* **112**, 214 (2016).
5. C. Yu, T. D. Nguyen, J. Q. Zhang, and D. J. Young, *Corrosion Science* **98**, 516 (2015).
6. Y. Xie, T. D. Nguyen, J. Zhang, and D. J. Young, *Corrosion Science* **146**, 28 (2019).
7. T. D. Nguyen, J. Q. Zhang, and D. J. Young, *Corrosion Science* **89**, 220 (2014).
8. Y. Cai, T. D. Nguyen, J. Zhang, B. Gleeson, and D. J. Young, *Corrosion Science* **210**, 110822 (2023).
9. Y. Cai, T. D. Nguyen, J. Zhang, B. Gleeson, and D. J. Young, *Corrosion Science* **195**, 110001 (2022).
10. Y. X. Xu, J. T. Lu, J. Y. Huang, W. Y. Li, J. B. Yan, X. W. Yang, and L. Yao, *Corrosion* **74**, 1446 (2018).
11. S. C. Okoro, M. Montgomery, F. J. Frandsen, and K. Pantleon, *Energy Fuels* **32**, 7991 (2018).
12. S. Liu, Z. Liu, Y. Wang, and J. Tang, *Corrosion Science* **83**, 396 (2014).
13. G. Salinas-Solano, J. Porcayo-Calderon, J. Gonzalez-Rodriguez, V. Salinas-Bravo, J. Ascencio-Gutierrez, and L. Martinez-Gomez, *Advances in Materials Science Engineering* **2014**, 1 (2014).
14. H. P. Nielsen, F. Frandsen, K. Dam-Johansen, and L. Baxter, *Progress in energy combustion science* **26**, 283 (2000).
15. R. Viswanathan and W. Bakker, *Journal of Materials Engineering and Performance* **10**, 81 (2001).
16. R. Viswanathan, J. Shingledecker, and R. Purgert, *Power* **154**, 41 (2010).
17. "FactSage 8.1 Thermochemical Software and Database (accessed July 2022)," ed (2022).
18. Y. Xie, Y. Cai, J. Zhang, B. Gleeson, and D. J. Young, *Oxidation of Metals* **95**, 23 (2021).
19. Y. Xie, Y. Cai, J. Zhang, B. Gleeson, and D. J. Young, *Corrosion Science* **181**, 109227 (2021).
20. C. Wagner, *Zeitschrift für Elektrochemie, Berichte der Bunsengesellschaft für physikalische Chemie* **63**, 772 (1959).
21. C. Wagner, *Journal of the Electrochemical Society* **99**, 369 (1952).
22. D. J. Young, *High Temperature Oxidation and Corrosion of Metals*, 2nd ed (Elsevier, New York, 2016),.
23. A. Sabioni, B. Lesage, A. Huntz, J. Pivin, and C. Monty, *Philosophical Magazine A* **66**, 333 (1992).
24. A. Sabioni, A. Huntz, L. Borges, and F. Jomard, *Philosophical Magazine* **87**, 1921 (2007).
25. I.-H. Jung, *Solid State Ionics* **177**, 765 (2006).
26. H. Grabke, E. Reese, and M. Spiegel, *Corrosion Science* **37**, 1023 (1995).
27. K. K. Aye, J. Zhang, and D. J. Young, *Oxidation of Metals* **94**, 2020 (51).
28. K. K. Aye, T. D. Nguyen, J. Zhang, and D. J. Young, *Corrosion Science* **179**, 109096 (2021).
29. K. K. Aye, Y. Cai, J. Zhang, and D. J. Young, *Oxidation of Metals* **97**, 371 (2022).
30. T. T. Sharobem, *Mitigation of high temperature corrosion in waste-to-energy power plants*. PhD thesis, Columbia University (2017).

31. Y. Kawahara, *Corrosion Science* **44**, 223 (2002).
32. R. Bender and M. Schütze, *Materials Corrosion* **54**, 652 (2003).
33. R. Bender and M. Schütze, *Materials Corrosion* **54**, 567 (2003).
34. W. S. Rasband, " ImageJ," *U.S. National Institutes of Health, Bethesda, Maryland, USA,* https://imagej.nih.govij/, 1997–2018.
35. R. P. Smith, *Transactions of the Metallurgical Society of AIME* **224**, 105 (1962).
36. C. Wells, W. Batz, and R. F. Mehl, *JOM* **2**, 553 (1950).
37. J. Lander, H. Kern, and A. Beach, *Journal of Applied Physics* **23**, 1305 (1952).